# Observations of Acoustic Noise Bursts Accompanying Nonlinear Internal Gravity Waves on a Continental Shelf off New Jersey

**Boris G. Katsnelson**[a]
Department of Marine Geosciences, University of Haifa, Haifa, Israel
**Oleg A. Godin**
Physics Department, Naval Postgraduate School, Monterey, CA 93943, USA
**Qianchu Zhang**
Department of Marine Geosciences, University of Haifa, Haifa, Israel

Running title: Acoustic noise of internal waves
Keywords: ambient noise; internal wave solitons; flow noise; sediment-generated noise; sediment transport

Submitted to the *Journal of the Acoustical Society of America* on November 30, 2020

[a] Electronic mail: bkatsnels@univ.haifa.ac.il

**Abstract**

Anomalously large, transient fluctuations of acoustical noise intensity, up to four-five orders of magnitude above the background, were observed with single hydrophone receiver units (SHRUs) and on the L-shaped horizontal and vertical line array of hydrophones (HVLA) in the Shallow Water 2006 experiment on the continental shelf off New Jersey. Here, temporal and spatial properties of these noise bursts are investigated. As tidally generated nonlinear internal waves (NIWs) move across the site of the experiment from the shelf break towards the coast, they form trains of localized, soliton-like waves with up to 25–35 m displacement of isopycnal surfaces. The NIW trains consecutively cross the positions of five SHRUs and HVLA that are located about 5–8 km from each other along a line perpendicular to the coast. The noise bursts were observed when an NIW train passed through locations of the corresponding acoustic receivers. Turbulence of the water flow, saltation and bedload of marine sediments were the dominant causes of the acoustic noise bursts caused by NIWs at different frequency bands. On near-bottom hydrophones, the most energetic part of the observed noise bursts is attributed to collisions of suspended sediment particles with each other, the sensor, and the seafloor.

## I. INTRODUCTION

Internal gravity waves in the ocean create time-dependent and spatially inhomogeneous variations in temperature and sound speed profiles and are known to have a significant effect on underwater sound propagation (Simmen et al., 1997; Colosi et al., 1999; Tang et al., 2007). Especially strong variations in the sound propagation conditions and attendant fluctuations of the acoustic fields occur due to nonlinear internal waves (NIW) on continental shelves (Zhou et al., 1991; Godin et al., 2006; Apel et al., 2007). The magnitude of the acoustic effects depends on the NIW amplitude and spatial structure as well as on the azimuthal direction of the acoustical track relative to the direction of NIW propagation, which determines the dominant physical mechanism of the NIW-sound interaction. For example, on a 14 km propagation track largely along NIW wavefronts in the SWARM95 experiment in the Mid-Atlantic Bight, NIW-induced focusing and defocusing of acoustic normal modes in the horizontal plane was found to result in sound intensity fluctuations of low-frequency (20–300 Hz), with magnitudes of 7–8 dB and periods of about 10 minutes (Badiey et al., 2002, 2007). In the same experiment, for mid-frequency signals (a few kHz) on a different sound propagation track crossing the NIW wavefronts, sound intensity fluctuations of a few dB took place due to NIW-induced coupling of the acoustic normal modes (Badiey et al., 2002; Katsnelson et al., 2009). Perhaps the strongest reported NIW-induced fluctuations of the transmission loss, or frequency-dependent sound intensity, of 20–25 dB were observed in the Yellow Sea off China; these were explained in terms of the resonant Bragg scattering of sound by an NIW wave train (Zhou et al., 1991; Apel et al., 2007).

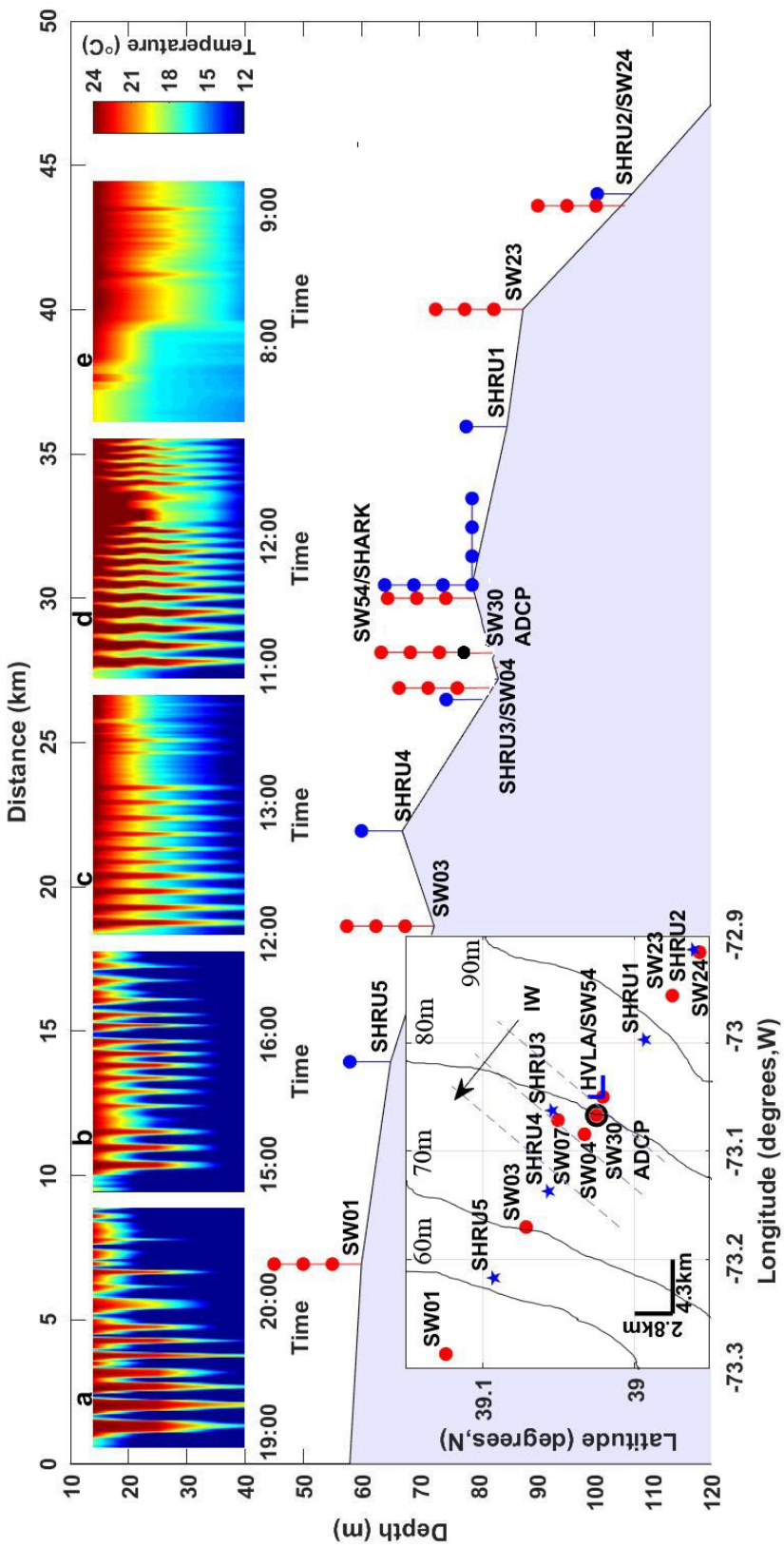


**Figure 1**. **(Color online)** Evolution of a train of nonlinear internal waves over the site of the Shallow Water 2006 (SW'06) experiment. Positions of thermistor chains SW01, SW03, SW04, SW07, SW23, SW 24, SW30, SW54, single-hydrophone acoustic receivers SHRU1, SHRU 2, SHRU3, SHRU4, SHRU5 and hydrophone array HVLA Shark as well as wave fronts (dashed lines) and the direction of propagation (arrow) of an internal wave train are indicated in the map in the lower left corner. Bathymetry is shown along the straight line through SW01 and SW24. ADCP is located at the SW30. Depth dependence of water temperature as measured by SW01 (**a**), SW03 (**b**), SW04 (**c**), SW54 (**d**), and SW23 (**e**) is shown from 07:00 to 21:00 GMT on 19 August 2006 when a train of nonlinear internal waves propagated shoreward from SW23 past SW01. Time (GMT) on 19 August 2006 is shown in hours and minutes

In addition to the propagation effects, NIWs were observed to change sound intensity by generating underwater acoustic noise. Currents of various nature, including NIW-induced currents, shed vortices and generate turbulent pressure fluctuations when flowing past acoustic sensors and elements of their moorings. These pressure fluctuations are observed as very low-frequency noise (typically, below a few tens of Hertz) and are known as flow noise (Strasberg, 1979; Webb, 1988). Measurements of NIW-induced flow noise have been described in the literature (Serebryany et al., 2008b; Yang et al., 2013). At higher frequencies, Serebryany et al. (2005, 2008a, 2008b) observed strong fluctuations of the ocean surface-generated broadband acoustic noise that accompanied passage of a strong NIW. These fluctuations were attributed to the modulation of the surface gravity and capillary-gravity wave activity on the ocean surface by NIW-induced currents. NIW-induced fluctuations of the intensity of the surface-generated noise reached 10–15 dB in deep water in the Indian ocean (Serebryany et al., 2005) and up to about 6 dB on the continental shelf in the in the Mid-Atlantic Bight (Serebryany et al., 2008b). Similar observations were made by Yang et al. in the Pacific northeast of Taiwan (Yang et al., 2013) and in the South China Sea (Yang et al., 2015), with about 10 dB variations of the acoustic noise intensity due to NIW-induced changes in the surface wave activity.

In the present paper, we describe our analysis of observations of very large (up to 50 dB) broadband, transient increases in the noise intensity, to be referred to as noise bursts, on the continental shelf off New Jersey. By combining acoustic observations on various hydrophones with measurements of the water temperature and current velocity, we established a relationship between individual noise bursts and tidally generated, localized, soliton-like NIWs, and identified the physical mechanisms likely responsible for the observed acoustic manifestations of the NIWs.

The paper is organized as follows: Section 2 outlines acquisition of the data used in this study. Properties of the noise bursts are discussed in Section 3. In Section 4 we show that the observed temporal and spectral characteristics of the noise bursts can be explained in terms of three physical mechanisms of noise generation, which include turbulence of the water flow and NIW-induced sediment saltation. Section 5 puts our findings into the broader context of previous research on sediment-generated underwater noise and sediment resuspension by NIWs. The results of the work are summarized in Section 6 along with their possible application to investigation of soliton-like NIWs on the continental shelf and of contributions of the NIWs to study of sediment transport and of soliton-like NIWs on the continental shelf.

## II. EXPERIMENT AND DATA

The data used in this study were obtained in the multi-disciplinary, multi-institutional Shallow Water 2006 experiment (SW'06). The experiment was carried out in July–September, 2006, in the Mid-Atlantic Bight on the continental shelf off New Jersey (Newhall et al., 2007; Tang et al., 2007; Lynch and Tang, 2008; Xue et al., 2014). A bathymetric map of the experiment site is shown in the lower left corner of Fig. 1. Water depth in this area decreases gradually from about 120 m near the shelf break to 55–60 m 40 km from the shelf break. The typical summer water temperature profile was characterized by a monotonic temperature decrease from the surface to the seafloor and a rather strong thermocline with about 12$^{o}$C temperature drop between 10 and 25 m depths. The corresponding sound speed profile was at its minimum on the seafloor and provided for a bottom-interacting guided sound propagation. However, occasional near-bottom intrusions of warm, salty water, sometimes referred to as "the foot of the shelfbreak front" (Linder and Gawarkiewicz, 1998), raised the sound speed minimum

to as high as the middle of the water column on some days during the observation period (Newhall et al., 2012).

The site of the experiment is characterized by a strong internal gravity wave activity, which is well documented (Tang et al., 2007; Shroyer et al., 2011; Xue et al., 2014). Approximately twice a day, a strong NIW is generated around the shelf break as a result of interaction of barotropic tides with the bathymetry. NIWs move from the shelf break shoreward in the northwest direction, largely along the bathymetry gradient. Over the two-month duration of the experiment, tens of events were registered of NIW train passages through the instrumented site. Direction of propagation and surface structure (shape of wavefronts, the number of waves in the train, and distance between them) were obtained using shipboard observations (Shroyer et al., 2011) and satellite images (Xue et al., 2014), which show a rather narrow spread of NIW propagation directions in the horizontal plane. NIW propagation directions were nearly parallel to the across-shelf line, along which a suite of acoustic sensors, thermistor chains, and acoustic Doppler current profilers (ADCPs) was deployed (Fig. 1).

Detailed information about the three-dimensional structure and temporal evolution of the NIW trains was obtained using a few tens of thermistor chains (Newhall et al., 2007; Tang et al., 2007; Lynch and Tang, 2008; Shroyer et al., 2011). These data show that the NIWs were predominantly depression waves except for possible reversal of polarity at shoaling that was observed (Shroyer et al., 2009) on several occasions. As semidiurnal internal tide moved from the shelf break towards the shore, each tidal internal wave evolved into a wave train consisting of up to 10–12 localized, soliton-like waves (Fig. 1). The isopycnal depression amplitude of the individual localized waves was largest near the leading front of the train and gradually decreased

toward its back end. The observed wave trains were qualitatively similar to the D-noidal model of NIWs (Apel, 2003).

Observations of strong NIW events on the 17, 18, 19 and 22 of August, 2006, have been selected for the present study. These events had quite similar patterns of NIW movement and, in turn, similar features of acoustic intensity fluctuations. Consider a 12-hour time period from 08:00–20:00 GMT on August 19, 2006. The period started with the appearance of an NIW in the shelf-break area. NIW evolution process can be analyzed using temperature records from a cluster of 16 thermistor chains in a 2x2 km square-shaped area (Newhall et al., 2007). Temperature was sampled at 30 s intervals. Positions of selected thermistor chains, denoted by letters SW, and of the acoustic receiving systems, single-hydrophone receiving units (SHRUs) and the L-shaped horizontal and vertical line hydrophone array (HVLA) Shark, are shown on the bathymetric map in Fig. 1. SHRUs were moored with heavy anchors, with the hydrophone located about 7 m above the seafloor. HVLA Shark consisted of a 16-hydrophone vertical linear array (VLA), which extended through most of the water column, and a 450m-long, 32-hydrophone, near-bottom horizontal linear array (HLA).

Five panels at the top of Fig. 1 show the temperature records obtained by five thermistor chains located at various distances from the shelf break. Each temperature record was 90 minutes long, corresponding to the time it took an NIW train to pass each thermistor chain. It can be seen that the NIW train was generated in the area between SW23 (where we can see the forward front of an unstructured NIW) and SW54, where NIW had developed a well-defined across-the-front structure. The distance between SW23 and SW24 was about 14 km. At SW54, the NIW contained 12 distinct, soliton-like waves (peaks of the depression of the isothermal surfaces) with amplitudes of the thermocline's displacement from equilibrium position of up to 25–30 m (Fig.

153 1). As the NIW train moved shoreward, it passed consecutively a set of acoustic receivers,
154 including the HVLA Shark and five SHRUs, which were located a distance of 5–8 km from one
155 other along a straight line. The NIW train evolved as it propagated; the amplitudes and the
156 number of the localized waves in the train changed (Fig. 1). One can estimate the speed $v$ of the
157 NIW train using distance between thermistor chains and the temporal interval between arrivals of
158 the NIW leading front. From such an estimate we obtained $v \sim 0.9$ m/s, length of the NIW trains
159 $L \sim 5$ km, quasi-period of the spatial structure inside the NIW train $l \sim 250$–300 m. The
160 corresponding scale of temporal variability was 5–7 minutes.

161 For the entire duration of the SW'06 experiment, acoustic pressure was continuously
162 measured by the SHRU and HVLA Shark hydrophones. The acoustic data was recorded with the
163 common sampling rate of 9765.625 Hz for all hydrophones. Measured time series $p(t)$ of
164 acoustic pressure $p$ are used below for calculation of various characteristics of the acoustic field,
165 including its intensity, frequency spectrum, and spectrograms. In addition, current velocity was
166 measured using acoustic Doppler current profilers (ADCPs). The data obtained with a moored
167 300 kHz ADCP (Fig. 1) that was used in this study is described in Section 3.

168 **III. OBSERVATIONS OF NOISE BURSTS**

169 The vertical line array of HVLA Shark was collocated with thermistor chain SW54 (Fig.
170 1) but other acoustic receivers, including SHRU1, SHRU4, and SHRU5, had no collocated
171 temperature sensors. Figure 2 presents a diagram demonstrating the connection between NIW
172 passage and observations of elevated noise intensity at different points across the shelf. In the top
173 panel, the vertical axis denotes distance along the straight line through locations of the
174 hydrophones and thermistor chains, with 0 of this axis corresponding to the position of the
175 thermistor chain SW01. The horizontal axis represents time and covers 15 hours of observations.

176 Temporal variation of temperature at different locations is illustrated by temperature
177 measurements (denoted by the letter ***t***), by one thermistor at 40 m depth of each of 5 thermistor
178 chains. Note that all positions of the forward front of NIW train in the range-time plane were
179 located approximately along a straight line, which indicates a nearly constant speed of the NIW
180 train of 0.9 m/s. Time series of measured sound intensity are shown for four SHRUs and one of
181 the hydrophones (channel 40) of HVLA Shark. The parts of these records that show large, rapid
182 increases (bursts) of the noise intensity are indicated by boxes ***a-e***. Figure 2 shows that the noise
183 bursts were observed when the NIW train traveled past the acoustic sensor.

184 More detailed information about the frequency content of acoustic signals and its time
185 dependence can be obtained using spectrograms. Spectrograms $S(f, t)$ have been calculated in the
186 frequency range 10-4000 Hz as follows:

187 $$\mathrm{S}(f, t_1) = \int W(t - t_1) p(t) e^{-i2\pi f t} dt \qquad (1)$$

188 Here $p(t)$ is a measured time series of acoustic pressure, $f$ is sound frequency, and $W(t–t_1)$
189 is the time window. A Kaiser window (Kaiser and Schafer, 1980) incorporating 1024 pressure
190 samples was used. Figure 2 shows spectrograms of noise recorded when a NIW train was
191 moving consecutively through positions of SHRU1 (panel ***a***), HVLA Shark (channel 40,
192 hydrophone in the center of HLA, panel ***b***), and SHRUs 3, 4, 5 (panels ***c, d, e*** , respectively).
193 HVLA Shark is represented in Fig. 2 by measurements on channel 40, which was a hydrophone
194 at the center of the horizontal line array.

195

196

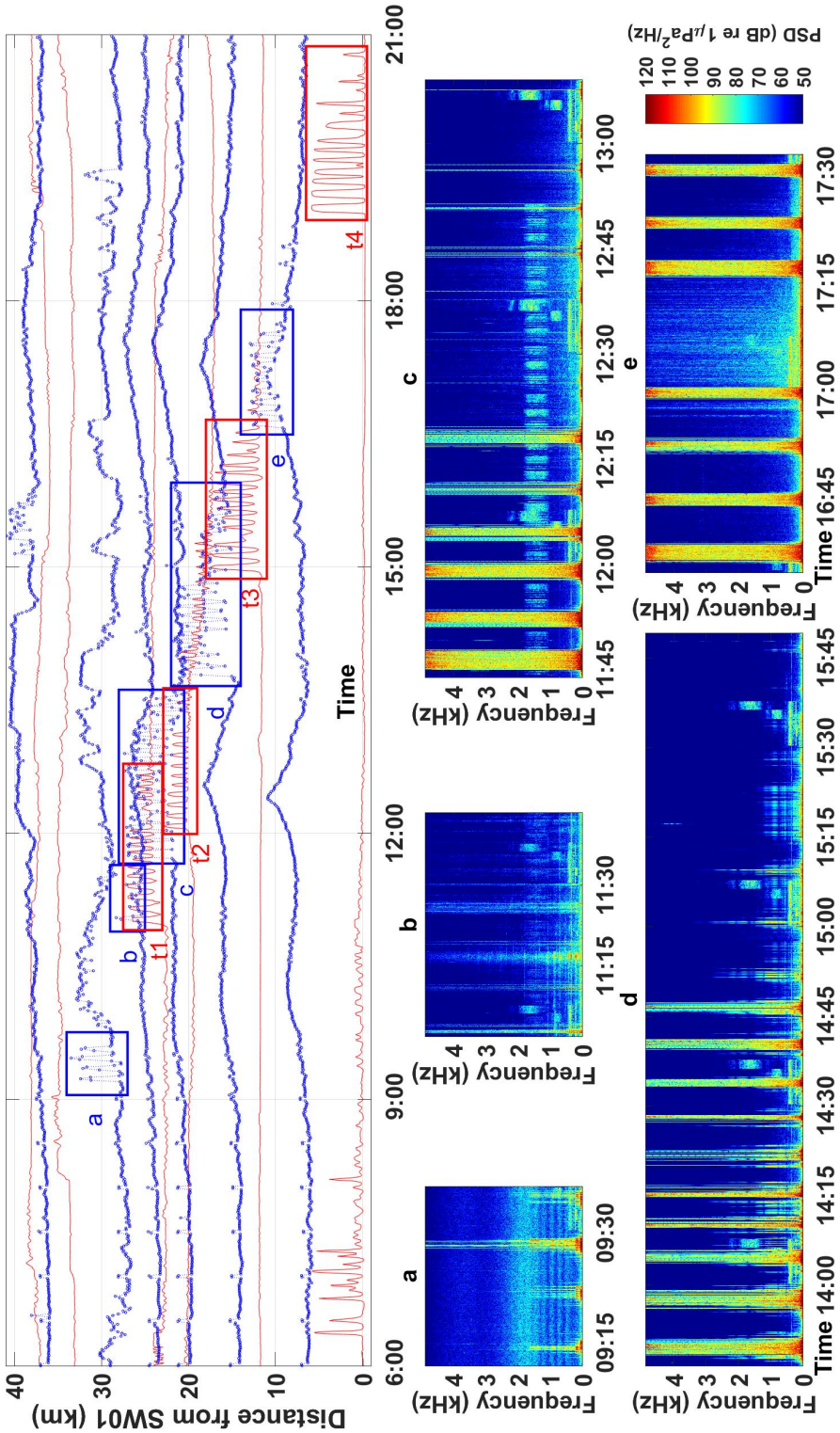


**Figure 2. (Color online)** Time histories of water temperature and acoustic intensity at various points along the path of propagating internal wave train. Temperature records of thermistors at the depth of 40 m are denoted by letter T and depicted in red for thermistor chains SW23, SW54, SW04, SW03, and SW01. Time intervals of appearance of the NIW train are denoted t1, t2, t3, t4 for the last four chains (SW23 does not show NIWs) and boxed. Sound intensity records by SHRUs 1, 3, 4, and 5 and hydrophone 40 of HVLA Shark are depicted in blue. For visibility, the time dependencies recorded by individual sensors are shifted vertically in proportion to the distance from the sensor to SW01. Time intervals with strong fluctuations of acoustic pressure are boxed and marked ***a*** for SHRU1, ***b*** for HVLA Shark, ***c*** for SHRU3, ***d*** SHRU4, and *e* SHRU5. Time (GMT) on 19 August 2006 is shown in hours and minutes. Five color panels in the lower part of the figure show the spectrograms corresponding to the sound intensity records in boxes ***a–e***.

197 In the area of NIW generation, where water depth was about 100 m, fluctuations of
198 acoustic intensity were relatively weak, especially at frequencies above 1 kHz (see panel ***a*** in
199 Fig. 2), although there was some correlation of the intensity fluctuations with NIWs. In
200 particular, the temporal scale of the sound variability of about 7 minutes corresponded to the
201 time interval between separate localized waves with the NIW train. A similar situation took place
202 on the HVLA Shark hydrophones (panel ***b***). Noise intensity was significantly weaker on the
203 vertical part of the L-shaped array than on its horizontal part as was previously reported by
204 Serebryany et al. (2008b).

205 Acoustic intensity fluctuations increased as the NIW train moved to shallower water.
206 Panel ***d*** in Fig. 2 depicts the spectrogram of noise recorded by SHRU4, which was located
207 between thermistor chains SW03 and SW04. Comparison of the shapes of the NIW train
208 recorded by these thermistor chains (panels ***b*** and ***c*** in Fig. 1) shows that the main parameters of
209 the NIW train – the number of individual localized waves, their amplitudes (~ 30–40 m), and the
210 time interval between the waves (~ 7 min) – did not change significantly between SW03 and
211 SW04. Hence, SW03 and SW04 measurements should provide a suitable representation of the
212 NIW train at SHRU4. Comparison of the temperature record ***c*** in Fig. 1 and spectrogram ***d*** in
213 Fig. 2 demonstrated a good agreement between the temporal scales (total duration of about 1
214 hour, the interval between peaks ~ 7 min) in the temperature and intensity measurements. The
215 agreement between time dependencies of the temperature variations and acoustic spectra
216 indicated a causal relation between NIWs and noise intensity fluctuations at SHRU4 and, by
217 extension, at other locations on the continental shelf.

218 The SW3 and SW4 temperature records (panels ***b*** and ***c*** in Fig. 1) have 12 large peaks,
219 which corresponded to individual localized internal waves. Amplitude of the waves tended to

decrease toward the tail of the NIW train. The data from acoustic sensors SHRU 3 and SHRU4, which were located between the thermistor chains SW3 and SW4 (Fig. 1), showed fewer peaks in the spectrograms. There are six strong, broadband noise bursts in SHRU3 data in panel ***c*** in Fig. 2. Water depth was about 68 m and 82 m at SHRU4 and SHRU3 locations respectively. For SHRU4, which was located in shallower water of 68 m depth, panel ***d*** in Fig. 2 shows 10 strong, broadband noise bursts. We relate the observed difference in the number of noise bursts to the difference in the speed of the near-bottom currents induced by NIWs at the two sites. As discussed in Section 4, speed of the near-bottom currents increased with increasing wave amplitude and decreasing water depth (see Eq. (4)). The change in the number of noise bursts at frequencies above a few hundred Hertz suggests that acoustic noise generation has a threshold character. Number of noise bursts is equal to number of the individual localized peaks in the NIW train with the speed of near-bottom current larger than threshold value.

The value of the threshold can be estimated by combining the noise intensity and water temperature measurements with current velocity data. Current velocity was not measured at acoustic sensor locations. We used the velocity data obtained with an acoustic Doppler current profiler, which was collocated with the thermistor chain SW30. Figure 3 compares the ADCP measurements with simultaneous measurements of the water temperature profile by thermistor chains SW07 and SW30 and acoustic observations at SHRU3. In the direction across the NIW wavefront, SW30 and ADCP preceded SHRU3 by about 700 m, and SW07 was behind SHRU3 by about 500 m (Fig. 1). This geometry was responsible for the 10–15 minutes shifts of the respective temperature and current velocity manifestations of an NIW wave train (Fig. 3b–d) from its acoustic manifestations (Fig. 3a). The wave train evolved as it propagated. Isothermal depressions had five and seven strong peaks following the leading front of the NIW train at

243 SW07 and at SW30, respectively (Fig. 3b, c). It is reasonable to assume that there were six
244 strong peaks at SHRU3, which is located between SW07 and at SW30. Figure 3a shows six
245 strong, broadband noise bursts following the leading front of the NIW train.

246

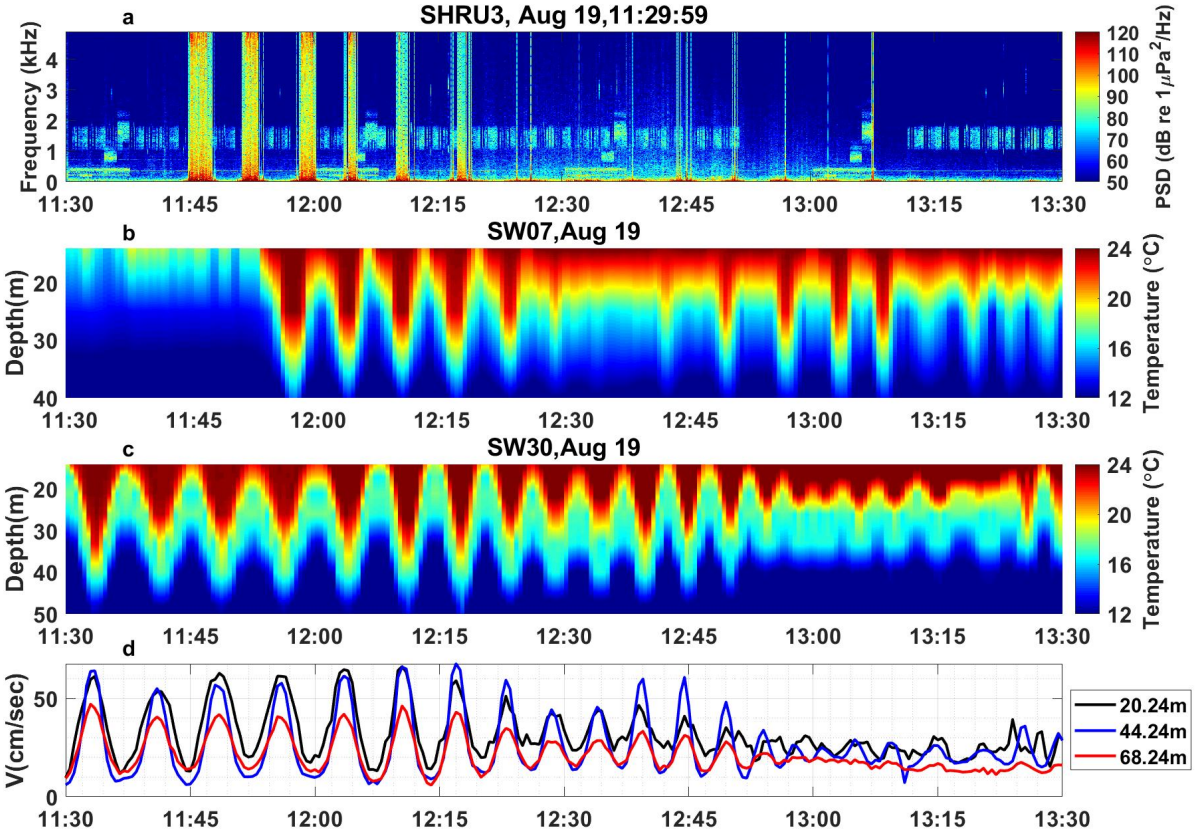


247

248 **Figure 3**. **(Color online)** Temperature, current velocity, and acoustic manifestations of an NIW
249 train in the vicinity of the acoustic receiver SHRU3. (**a**) Spectrogram of acoustic noise recorded
250 by SHRU3. (**b**) Time history of the water temperature on the thermistor chain SW07. (**c**) Time
251 history of the water temperature on the thermistor chain SW30. (**d**) Time-dependence of the
252 horizontal current velocity at three depths: 20.2 m (1), 44.2 m (2), and 68.2 m (3). Time (GMT)
253 on 19 August 2006 is shown in hours and minutes.

254

255 Horizontal velocity of the water flow caused by the NIW train reached its maximum
256 when the isothermal depression was at maximum (Fig. 3c, d). Observed velocities reached – and
257 for the strongest peaks exceeded – 60 cm/s below the thermocline. Velocity magnitude gradually
258 declined with depth below the thermocline and decreased by a factor of about 1.5 near the
259 bottom (Fig. 3d). Comparison of the spectrogram of acoustic noise with the ADCP
260 measurements indicated that strong, broadband noise bursts occurred when the NIW-induced
261 near-bottom current exceeded a threshold value of about 40 cm/s.

262 These results suggest that the noise bursts occurred around the time when a peak of
263 isothermal depression passed the observation point. A more precise relation between the phase of
264 the isothermal displacement and acoustic noise can be obtained using the HVLA Shark data,
265 since SW54 thermistors were attached to the vertical part of the hydrophone array. Figure 4
266 compares simultaneous, collocated measurements of the water temperature profile and sound
267 intensity on the lowest hydrophone on the vertical part of the array. The figure demonstrates that
268 maximum noise intensity was observed when the NIW-induced displacement of isothermal
269 surface was at maximum. The time-dependent acoustic intensity *I* and intensity level *IL* were
270 calculated as follows:

271 $$I(t_1) = \frac{1}{2\rho c \Delta t}\int_{t_1}^{t_1+\Delta t}|p(t)|^2 dt\ , \tag{2}$$

272 $$\mathrm{NIL}(t_1) = 10\log_{10}[\frac{I(t_1)}{I_0}] \tag{3}$$

273

Here $\Delta t$ = 1 s is the average time, $\rho$ and $c$ are the density and sound speed in water, and $I_0$ is the reference intensity, corresponding to the root mean square acoustic pressure of 1 μPa.

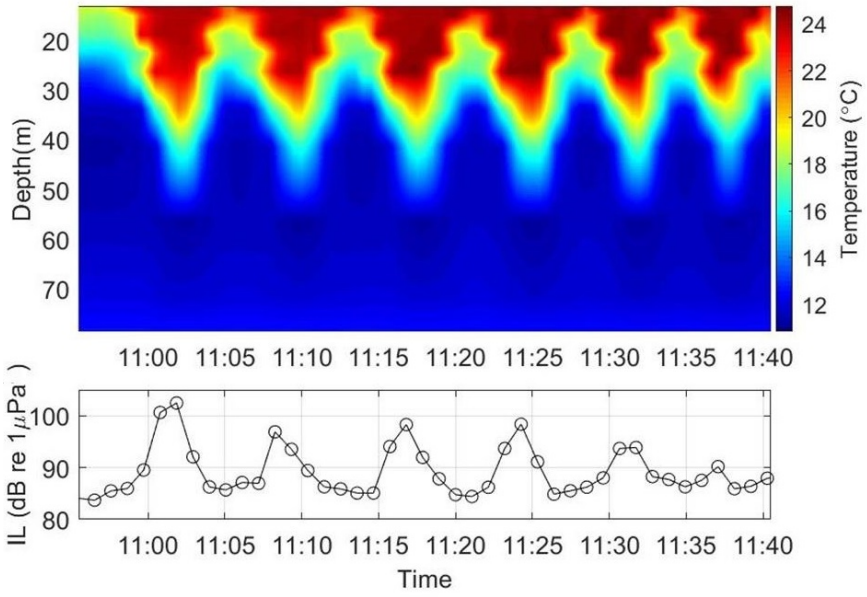


**Figure 4**. **(Color online)** Temporal variations of the temperature depth dependence measured by thermistor chain SW54 (upper panel) and noise intensity on a collocated hydrophone (lower panel). Time (GMT) on 19 August 2006 is shown in hours and minutes.

The noise generated by NIWs on near-bottom hydrophones was as strong as, if not stronger, than any signal received or noise of a different origin. This is illustrated in Fig. 5, which shows the time dependence of acoustic intensity recorded by SHRU5 during a full day. A number of sound generation mechanisms contributed to the observed acoustic field. For instance, from 04:00 to 17:00 there were prominent signals from the research sources (Newhall et al., 2007; Lynch and Tang, 2008), which were towed through the experiment site. Strong low-frequency noise, presumably due to shipping and/or a storm, was present from about 10:00-14:00. This noise was superimposed on and overshadows signals from the research sources. NIW-induced noise intensity bursts appeared as a sequence of high and narrow, quasi-periodic

intensity peaks in the 16:30-17:30 time interval. Intensity of the noise bursts reached 150-155 dB re 1 μPa. It exceeded the background noise intensity of 110-115 dB re 1 μPa by 40 dB, or four orders of magnitude.

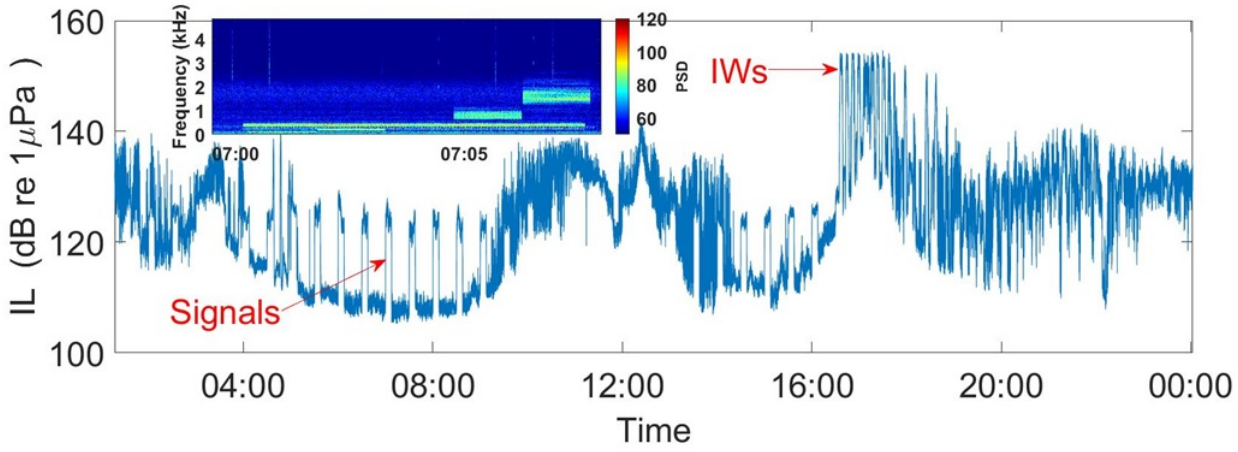


**Figure 5**. **(Color online)** Temporal variation of the acoustic intensity measured by SHRU5. Time (GMT) on 19 August 2006 is shown in hours and minutes. The insert shows the spectrogram of a nine-minute section of the pressure record and illustrates contributions of research sound sources. Color shows power spectral density of total acoustic field in dB re 1 $\mu Pa^2/Hz$.

## IV. MECHANISMS OF NOISE GENERATION

Noise intensity, its time dependence, and the spectral content of the noise showed significant variability depending on hydrophone position and position of NIW train. Three distinct types of acoustic noise that accompanied the passage of NIWs can be identified, which combined to explain the bulk of observations (see Fig. 6). These types are (i) low-frequency noise, which is illustrated in Figs. 6a and 6b, (ii) noise spikes of ~1 s duration with spectral peaks

304 located below approximately 1 kHz (Fig. 5c), and (iii) more frequent, shorter-duration spikes
305 with prominent high-frequency content above 3 kHz, which subsequently merged to become a
306 continuous signal of a few minutes in duration (Fig. 6d).

307 The low-frequency noise was most pronounced at infrasonic frequencies below 10 Hz
308 (Fig. 6b). It was observed almost continuously as each soliton-like wave in the NIW train passed
309 the acoustic receiver. Acoustic intensity increased rapidly with the magnitude of pycnocline
310 depression (see the time dependence of noise spectral density at frequencies below 10 Hz in Fig.
311 6b). The low-frequency noise was clearly observed on all SHRUs and on VLA hydrophones,
312 where noise intensity was only weakly dependent on the hydrophone depth.

313 We interpret the low-frequency noise that was observed as flow noise (Strasberg, 1979;
314 Webb, 1988; Bassett et al., 2014). Flow noise, also known as pseudosound, results from
315 advection of pressure fluctuations in a turbulent flow past the sensor. Pressure fluctuations
316 include ambient fluctuations in a turbulent flow as well as pressure pulsations due to eddy
317 shedding when the flow interacts with the sensor and the entire mooring. Intensity of flow noise
318 is known to increase with decreasing frequency (Strasberg, 1979; Webb, 1988; Bassett et al.,
319 2014). Interpretation of the low-frequency noise as flow noise is supported by the apparent
320 absence of such noise in signals on HLA hydrophones, which lie on the seafloor. For the
321 pseudosound due to eddy shedding, by the flow past a cylinder of diameter $d$, the representative
322 frequency is $f_e = St\, u/d$, where $St \sim 0.2$ is the Strouhal number and $u$ is flow velocity (Strasberg,
323 1979; Webb, 1988). With NIW-induced currents of ~0.5 m/s (Serebryany et al., 2008b; see also
324 Fig. 3d), the observed upper frequency of 10 Hz is consistent with the eddy shedding by a
325 mooring wire with $d \sim 1$ cm. The hydrophone and pressure housing have larger dimensions and
326 contribute to lower-frequency pseudosound.

327 The observed strong correlation between intensity of low-frequency noise and pycnocline
328 depression in NIWs (Fig. 4) can be understood within the following simple model of NIW
329 currents. Consider a progressive NIW with a linear wavefront, which moves with speed $c$ along
330 horizontal coordinate $x$ in an ocean, where potential density jumps across a narrow pycnocline
331 and remains constant below it. Let the water depth, unperturbed pycnocline depth, and
332 pycnocline depression due to NIW be $H(x)$, $h(x)$, and $\eta(x - ct)$. The flow is stationary in the
333 reference frame moving with NIW. In the long-wave approximation (Apel et al., 2007), it
334 follows then from the continuity equation that flow velocity $u(x, t)$ below the pycnocline is

335 $$u = \frac{-c\eta(x-ct)}{H(x)-h(x)-\eta(x-ct)} \quad (4)$$

336 The minus sign in the numerator in Eq. (4) indicates that near the seafloor, water flows in
337 the direction opposite to the direction of NIW propagation. Note that magnitude $|u|$ of the flow
338 velocity rapidly increases with increasing pycnocline depression and, for fixed $\eta$, is inversely
339 proportional to the distance from the perturbed pycnocline to the seafloor. For example, in the
340 vicinity of SHRU3 the water depth was $H \approx 80$ m, thickness of thermocline $h \approx 20$ m and the
341 pycnocline depression $\eta \approx 20$ m, and Eq. (4) gives $|u| = c/2 \sim 0.5$ m/s. This estimate agrees well
342 with the ADCP measurements shown in Fig. 3d.

343 The key to understanding the origin of the second noise type, illustrated in Fig. 6c, is the
344 fact that it was observed only on HLA hydrophones and was not present on either VLA
345 hydrophones or SHRUs. HLA hydrophones lay on the seafloor, while the VLA and SHRU
346 hydrophones were located at least 6 m above it. Moreover, the type-two noise was at maximum
347 on hydrophones in the middle of the HLA, and no noise of this type was observed on the
348 hydrophones at both ends of the array, which were fixed by heavy anchors (Newhall et al.,

2007). All the observed features of type-two noise are consistent with hydrophones being dragged along the seafloor by NIW-induced near-bottom currents, with the stronger noise caused by the bigger displacements that occurred away from the anchors. This interpretation was proposed by Serebryany et al. (2008a, 2008b), who were the first to report observations of NIW-associated noise on several HLA hydrophones in the middle of the array.

The third and most intense type of observed noise is illustrated in Fig. 6d, which uses the SHRU5 data. We interpret this noise type as the noise generated by moving sediments that had been mobilized by the NIW-induced near-bottom currents. After sediment particles leave the seafloor, they generate acoustic waves (noise) by colliding with each other and with the stationary seabed as well as with near-bottom acoustic sensors and/or their housing. Mobilization of sediments and dynamics of the suspended sediment particles are controlled by the composition of surficial sediments and the near-bottom current velocity.

361

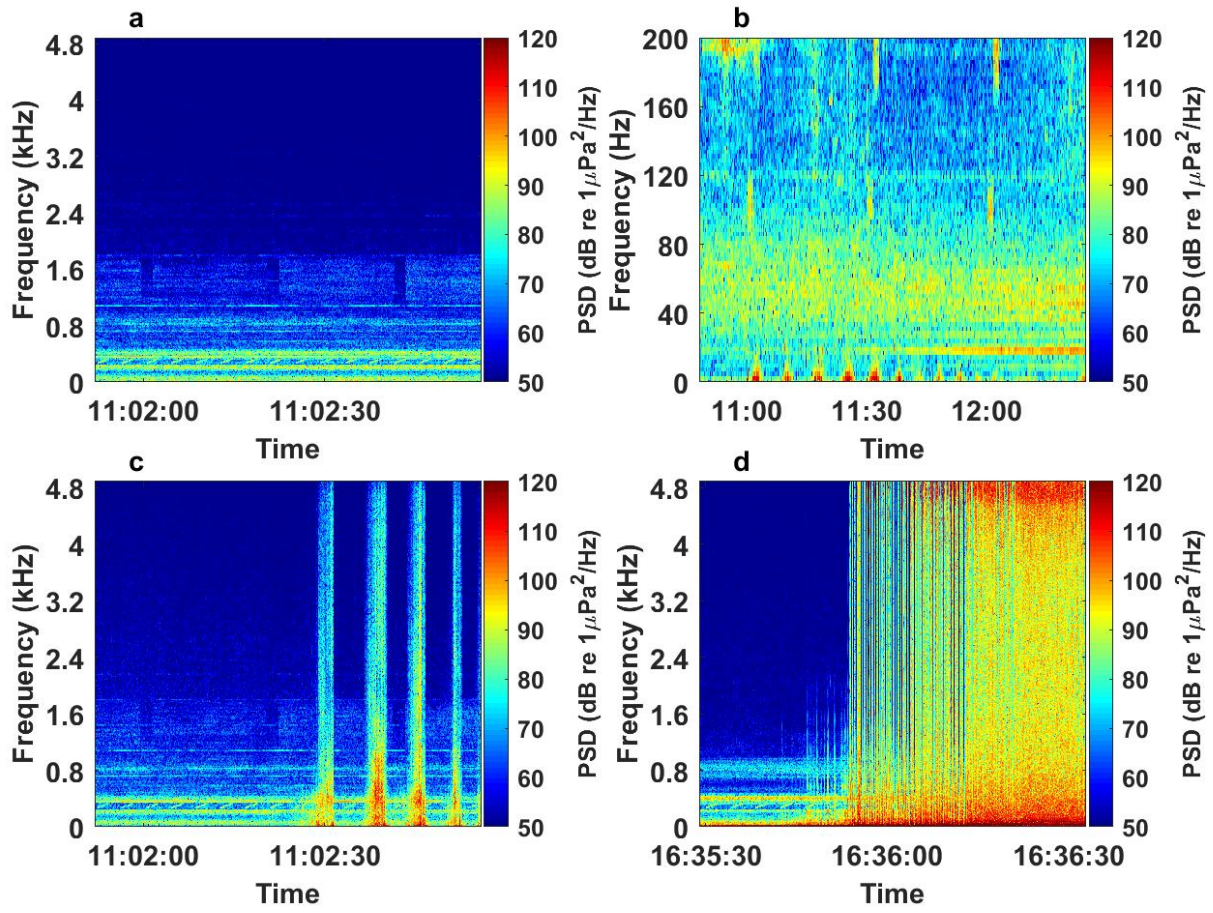


362 **Figure 6**. **(Color online)** Spectrograms of acoustic field recorded by hydrophones on vertical
363 (VLA) and horizontal (HLA) arrays during passage of a train of nonlinear internal waves.
364 Spectrograms are shown of acoustic pressure on a VLA hydrophone at depth of 62 m (**a**); low-
365 frequency part of the acoustic pressure on the same hydrophone (**b**); on a hydrophone in the
366 middle of HLA (**c**); and on single-hydrophone receiver SHRU5 (**d**). Time (GMT) on 19 August
367 2006 is shown in hours minutes, and seconds.

368

369 To our knowledge, NIW-induced sediment generated noise (SGN) has not been
370 previously described. [The possibility of occurrence of such noise was hypothesized by
371 Serebryany et al. (2008b) and Yang et al. (2015).] However, there is extensive literature on SGN

372 produced by other kinds of currents such as river flow, orbital velocities in surface gravity
373 waves, and tidal currents (Bassett, 2013; Thorne, 2014; Rickenmann, 2017). SGN has been
374 measured using underwater sensors and seismometers on dry land (Roth et al., 2016). SGN
375 properties have been studied in laboratory experiments (Thorne, 1985, 1986), in rivers (Roth et
376 al., 2016; Geay et al., 2017; Petrut et al., 2018) as well as in straits (Thorne, 1986; Bassett, 2013)
377 and the surf zone at sea (Voulgarist et al., 1999). Bassett et al. (2013) investigated SGN caused
378 by currents in a tidal channel in Puget Sound. They found that a near-bottom current velocity
379 above a critical value of 50–60 cm/s was necessary to produce SGN and that the shape of the
380 SGN spectrum depended on sediment grain size. SGN was typically most pronounced above 2
381 kHz with a maximum spectral density at frequencies of 10–15 kHz.

382 The threshold character, frequency content, and the value of the current velocity
383 threshold (Section 3) of the type-three NIW-induced noise are consistent with the previously
384 observed SGN due to tidal currents in the ocean, which supports our interpretation of the
385 mechanisms of the type-three noise. The difference in the current velocity thresholds (~40 cm/s
386 vs. 50–60 cm/s) can be attributed to a difference in the sediment grain sizes at the experiment
387 sites on the New Jersey shelf and in Puget Sound.

388 Let us compare quantitatively the conditions, under which the third noise type was
389 observed, with the conditions (e.g., Miller et al., 1977; Wiberg and Smith, 1987) needed for
390 sediment mobilization to occur at the SW'06 experiment site. Sediment grains begin to move and
391 SGN arises when the shear stress due to near-bottom current exceeds a certain threshold. The
392 shear stress and the threshold (critical) shear stress are usually characterized in terms of the
393 shear, or friction, velocity $u_*$ and its critical value $u_*^{cr}$. Experimentally determined dependence
394 of $u_*^{cr}$ on the grain size $D$ of well-sorted, siliciclastic sediments (the Inman curve) can be found in

(Miller et al., 1977) and, with additional experimental results, in (Wiberg and Smith, 1987). It is reproduced in Fig. 7a (curve 5). A semi-empirical theory of the critical shear stress is presented by Wiberg and Smith (1987) for sediments consisting of either grains of the same size or a mixture of grains of different sizes. The seabed roughness, which affects the turbulent flow in the near-bottom boundary layer, is characterized in this theory by the roughness scale length $k_s$. For well sorted (uniform) sediments, $k_s = D$; for poorly sorted sediments, which contain a range of grain sizes, $k_s$ can be evaluated as the 65$^{th}$ percentile, $D_{65}$, of the grain size distribution (Wiberg and Smith, 1987). In poorly sorted sediments, mobilization conditions are different for grains of different size. Lines 1–4 in Fig. 7a show the threshold shear velocities $u_*^{cr}$ vs. the grain size $D$ for several values of the seabed roughness scale $k_s$. These curves are calculated as a product of the $u_*^{cr}$ value at $D = k_s$, which is given by the Inman curve, and the square root of the theoretically predicted ratio of the critical shear stresses at a given value of the ratio $D/k_s$ and at $D/k_s = 1$. The shear stress ratio had been calculated by Wiberg and Smith (1987) as a function of the critical roughness Reynolds number $u_*^{cr} k_s / \nu$, where $\nu$ is the kinematic viscosity of water, for a discrete set of $D/k_s$ values and was taken from Fig. 7 in (Wiberg and Smith, 1987). Note that $u_*^{cr}$ increases monotonically with increasing $D$, when $D = k_s$, see the Inman curve (curve 5) in Fig. 7a, and decreases when the ratio $D/k_s$ increases (Wiberg and Smith, 1987). For each fixed roughness scale, in the range of $k_s$ values represented in Fig. 7a the product of the steadily increasing and the steadily decreasing function of grain size $D$ results in the dependence of $u_*^{cr}$ on $D$, to be referred to as a modified Inman curve, which has a minimum at a certain grain size, see curves 1–4 in Fig. 7a. The minimum value is less than the value at the point $D = k_s$, where the modified

Inman curve and the Inman curve intersect. Hence, mobilization of the poorly sorted seabed starts at a smaller current velocity than of a well sorted seabed with the same roughness scale.

Assuming that the theory of Wiberg and Smith (1987) applies to a mixture of grains with a wide range of sizes, the modified Inman curves in Fig. 7a indicate that poorly sorted sediments become mobilized when the shear velocity of the near-bottom current exceeds the minimum of the modified Inman curve calculated for the roughness scale $k_s$ of that particular seabed. Only grains with the size that minimizes the respective modified Inman curve are mobilized at first; mobilization of grains in an increasingly wider range of $D$ values occurs when $u_*$ rises further above its minimum on the modified Inman curve.

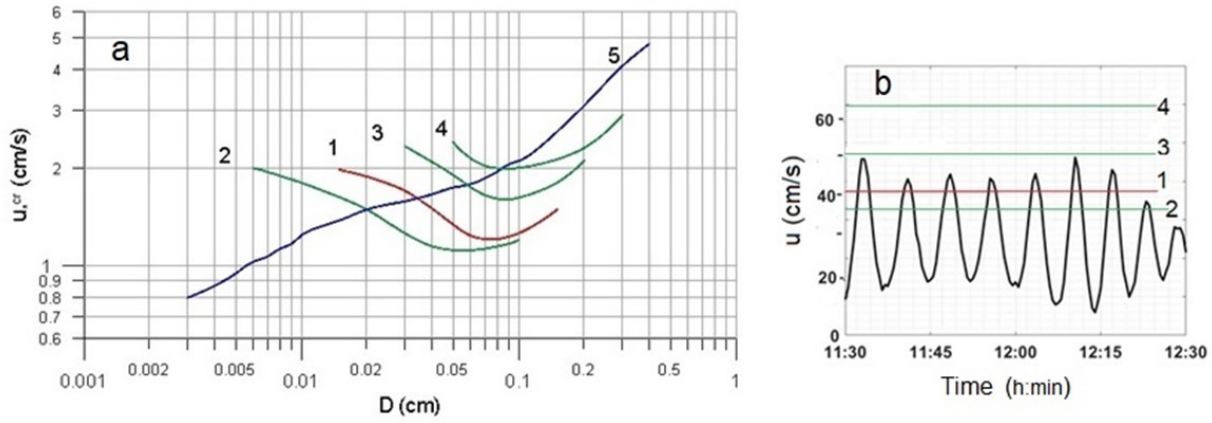


**Figure 7. (Color online)** Theoretical estimates of the threshold of sediment mobilization by near-bottom currents. **(a)** The minimum value $u_*^{cr}$ of the shear velocity $u_*$ that leads to mobilization of sediment grains of size $D$ is depicted under the conditions of the SW'06 experiment, where $k_s$ = 0.035 cm (1), and for seabeds with three other roughness scales: $k_s$ = 0.02 cm (2), 0.07 cm (3), and 0.10 cm (4). The threshold $u_*^{cr}$ values are calculated following Wiberg

and Smith (1987). Also shown is the Inman curve (5), which gives an experimentally determined $u_*^{cr}$ for well-sorted seabeds with $k_s = D$. The Inman curve is adapted from (Miller et al., 1977) and (Wiberg and Smith, 1987). **(b)** ADCP-measured time-dependence of the horizontal current velocity at depth of 68.3 m. Thin horizontal lines show theoretical values of the minimum current velocity required for mobilization of the poorly sorted sediments of the four different sediment types considered in (a). Time (GMT) on 19 August 2006 is shown in hours and minutes.

Sediment material properties on the New Jersey shelf, including the SW'06 site, have been investigated by Goff et al. (2004). With respect to locations of our acoustic and current velocity measurements, the two closest points, where grab samples were taken by Goff et al. (2004), are at 73.07922 °N, 39.04995 °W and 73.05421 °N, 39.03689 °W. These points are within 2 km from where the acoustic and current velocity data illustrated in Figs. 3a and 3d were obtained. The seafloor sediments are siliciclastic, and their size distribution was classified by Goff et al. (2004) as "high fine/low coarse." A representative histogram of the size distribution for this sediment type is given in Fig. 3 in (Goff et al., 2004). The size distribution is rather broad. The histogram peaks between 250 μm and 375 μm, with the average grain size of 293 μm and 20.1% and 1.1% by weight, respectively, of the fine ($D < 63$ μm) and coarse ($D > 4000$ μm) grains. We used the histogram to find $D_{65} \approx 350$ μm.

To relate the theoretical conditions of the onset of sediment motion to observed NIWs, we utilize the ADCP current measurements (Fig. 3d) at the largest available depth of 68.3 m, or 17.7 m above the seabed. Line 1 in Fig. 7b depicts the modified Inman curve for the seabed roughness scale $k_s = D_{65} = 0.035$ cm expected at the sites of the SHRU3 and ADCP

455 measurements that are shown in Figs. 3a and 3d. At elevations $z$ above the seabed, which are
456 much larger than $k_s$, the flow velocity profile in the boundary layer is logarithmic:

457 $$u(z) = \kappa^{-1} u_* \ln(z/z_0) \quad (5)$$

458 where von Karman's constant is $\kappa = 0.407$, and $z_0 = k_s/30$ (Wiberg and Smith, 1987).

459 To verify that the logarithmic velocity profile model is appropriate at the depths, where
460 the ADCP data is available, we followed Lueck and Lu (1997) and Bassett et al. (2013) and
461 characterized the accuracy of the logarithmic regression of the measurements up to different
462 elevations above the seabed in terms of the coefficient of determination $R^2$. Measured horizontal
463 current velocity profiles during the NIW passage on 19 August 2006 (Fig. 3) were retrieved with
464 30 s intervals. The ADCP measurements with horizontal current velocity of at least 35 cm/s at
465 the deepest point were selected for analysis. These measurements correspond to time intervals
466 around the time of passage of peaks of soliton-like waves and include all the times, when
467 sediment mobilization by NIWs was expected to occur. The logarithmic approximation was
468 found to be applicable up to 30–35 m above the seabed, with $R^2 > 0.8$ for all current velocity
469 profiles and $R^2 > 0.9$ for 88% of the measurements. Larger $R^2$ typically corresponded to stronger
470 currents.

471 Equation (5) was used to relate the minima of the threshold values $u_*^{cr}$ in Fig. 7a, which
472 are equal to 1.2, 1.1, 1.6, and 2.0 cm/s on lines 1–4, respectively, to corresponding current
473 velocities of 40 cm/s, 38 cm/s, 52 cm/s, and 63 cm/s at depth of 68.3 m in Fig. 7b. The sediment
474 at SHRU3 site is expected to become mobilized when the measured current velocity reaches 40
475 cm/s. This condition is met for the first seven soliton-like waves in the NIW in Fig. 7b. Grains
476 with sizes between 700 and 800 μm will be mobilized first, see Line 1 in Fig. 7a. Such grains are

477 present at a considerable level in the measured size distribution in (Goff et al., 2004). As the
478 current velocity increases to 50 cm/s in the first soliton-like wave, the mobilization threshold $u_*^{cr}$
479 is exceeded in a wider range of the grain sizes (Fig. 7a), which includes a part of the maximum
480 of the size distribution at $D$ >350 μm.

481 Figure 3a shows six periods of the type-three noise occurrence at SHRU3 rather than the
482 seven peaks predicted based on the ADCP measurements. As has been discussed in Section 3,
483 the difference between the number of the strong peaks in the current velocity (Fig. 3d) and
484 acoustic (Fig. 3a) measurements can be attributed to the NIW train evolution on its path from the
485 ADCP to SHRU3.

486 The predictions of sediment mobilization by the NIW are rather sensitive to the grain size
487 distribution. For coarser sediments with the seabed roughness length of 0.070 cm or 0.100 cm
488 instead of $k_s$ = 0.035 cm derived from the Goff et al. (2004) measurements, the observed NIW-
489 induced currents are not strong enough to mobilize the sediments (Fig. 7b). In contrast, if
490 sediments were finer and had $k_s$ = 0.020 cm, it would increase the number of soliton-like waves
491 in the observed NIW train that mobilize that sediments, see Line 1 in Fig. 7b. If the sediments
492 had the same mean grain size of 293 μm as at the SW'06 site but were well sorted, estimate of
493 $u_*^{cr}$ from the Inman curve gives the critical current velocity of 55 cm/s at depth of 68.3 m, which
494 exceeds the NIW-induced currents in Fig. 7b. Hence, no sediment mobilization would occur in
495 that case.

496 Because of the uncertainties in the knowledge of the sediment properties at the exact site
497 of acoustic observations and current measurements; due to SHRU 3 and the ADCP not being co-
498 located; as well as because of the assumptions and approximations inherent to the Wiberg and

499 Smith theory, the derived value of 40 cm/s for the threshold current velocity should be viewed as
500 an estimate rather than an accurate prediction. Nevertheless, the close agreement between the
501 model of the onset of sediment mobilization and acoustic observations of the emergence and
502 disappearance of the type-three noise is remarkable. The quantitative agreement between the
503 conditions of the occurrence of the type-three acoustic noise and the sediment entrainment
504 strongly supports our interpretation of this noise type as SGN.

505 Figure 8 compares power spectra and intensity of the NIW-induced noise on three
506 hydrophones, where one of the three noise types dominates. We used the data obtained with
507 SHRU5, one VLA hydrophone, and one HLA hydrophone. These are the same sensors that were
508 used in Fig. 6 to illustrate the differences between the three noise types. Power spectra of the
509 background ambient noise are usually modeled using the well-known Wenz curves (Wenz,
510 1962). When there were no NIWs in the vicinity of the sensors, all three hydrophones recorded
511 signals with rather similar spectra at all frequencies above 10 Hz (Fig. 8a). The measured spectra
512 were close to the Wenz curve if contributions of the spectral peaks due to linear frequency
513 modulated signals around 300 Hz and 500 Hz and other signals emitted by known research
514 sound sources are excluded (Newhall et al., 2007; Lynch and Tang, 2008).

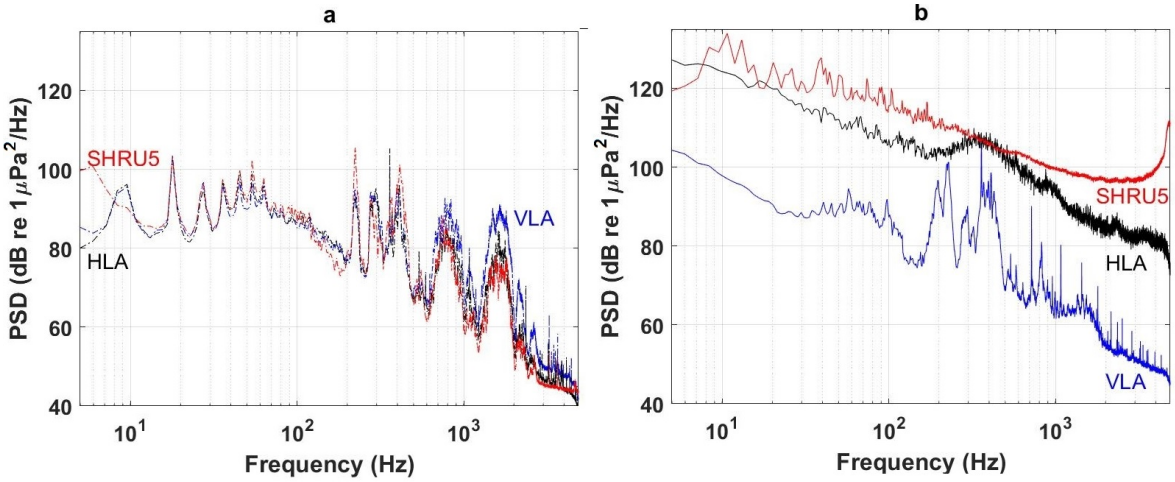

515 **Figure 8**. **(Color online)** Power spectra of acoustic pressure recorded by SHRU5 and
516 hydrophones on vertical and horizontal arrays when nonlinear internal waves are absent (**a**) or
517 present (**b**). The power spectra are calculated for the same hydrophones as in Fig. 6.

518

519 In the presence of an NIW train (Fig. 8b), the spectrum of the acoustic pressure on the
520 VLA hydrophone did not change appreciably, except at frequencies below 10 Hz. This is
521 consistent with the flow noise properties. Signals from the research sources could still be clearly
522 seen above the noise background. In contrast, very strong, broadband increase of noise level
523 (Fig. 8b) occurred on HLA, which was dragged along the seafloor by the NIW-induced current.
524 The spectrum retained manifestations of the research sources in the 300–1000 Hz frequency
525 band. At SHRU5, where the velocity of the NIW-induced near-bottom current exceeded the
526 threshold for type-three noise generation, there was a broadband increase of the spectral level of
527 about 30 dB between 10 Hz and 2 kHz and a rather sharp increase of the spectral level (up to ~
528 40-50 dB relative to the background noise level) at frequencies above 2 kHz (Fig. 8b). The
529 spectral maximum occurred at frequencies above the highest frequency that can be resolved with
530 the 9765.625 Hz sampling rate of the SHRU5 measurements, as expected for sediment generated
531 noise (Thorne, 1986; Bassett et al., 2013; Petrut et al., 2018). At SHRU5, NIW-induced SGN
532 surpassed contributions of all other sources of sound at every frequency.

533 The increase due to type-three noise in the spectral level of the sound observed at SHRU5
534 (Fig. 8) is larger and extends to lower frequencies than in other oceanic observations reported by
535 Thorne (1986) and Bassett et al. (2013) for comparable and even stronger near-bottom currents.
536 SGN intensity is often considered to be a measure of sediment transport rates (Thorne, 1986,
537 2014; Voulgarist et al., 1999) for a given sediment and instrument type. However, it is harder to

compare SGN levels created by different sediments and measured by dissimilar instruments. Noise at SHRU5 may have been enhanced by the vertical advection of entrained sediment particles by NIW currents or by direct impacts of these particles on the hydrophone or elements of the mooring. Furthermore, the sharp increase in the noise spectral level at the highest resolved frequencies and extension of the type-three noise well below 1 kHz (Fig. 8b) suggest the possibility of aliasing of higher-frequency SGN energy into the observation band. These possible contributions to the observed noise spectrum can be neither excluded nor quantified with the available SW'06 data. In view of these uncertainties as well as significant differences in the sediment composition between different sites, the larger effect of sediment mobilization on noise spectral levels at SHRU5 than in the previous observations (Thorne, 1986; Bassett et al., 2013) should not be interpreted to mean that the NIW-induced sediment transport on continental shelf is stronger than the sediment transport in tidal channels.

## V. DISCUSSION

As mentioned in Section 2, in the six weeks of SW'06 acoustic measurements, a few tens of strong NIW trains were detected. During the six-day period from 17 – 22 August 2006 chosen for this study, strong NIW trains and attendant noise bursts were observed three more times in addition to the 19 August 2006 event analyzed above. A particularly large NIW train, which contained 11 soliton-like waves with large amplitudes, occurred at nighttime on 17–18 August 2006. The noise bursts generated by this wave train were registered on SHRU3, SHRU4, and SHRU5 with the acoustic intensity and spectrograms rather similar to those measured on August 19. Weaker NIW trains, with only three prominent soliton-like waves and of smaller amplitude, were observed on August 18 and 22. The noise bursts accompanying these NIW trains were detected on SHRU4 and SHRU5 but not SHRU3 and had lower acoustic intensity than on

August 19. The spectrograms of the noise bursts observed by the SHRUs during the three NIW events revealed contributions of the low-frequency type-one, or flow, noise and the high-frequency type-three noise, which we interpret as SGN.

SGN is an acoustic manifestation of sediment mobilization by water flow. While NIW-induced SGN apparently has not been studied previously, there exists a large body of work on the effects that NIWs have on marine sediments on the continental shelf, and there is no doubt that sediment mobilization by NIWs does occur. It is known that the boundary layer at the footprint of NIW can became hydrodynamically unstable, and this instability results in an increase of the sediment resuspension rate (Carr and Davies, 2006). Moreover, any increase in the turbulent energy due to the hydrodynamic instability can maintain a higher sediment concentration in the water column. Bogucki et al. (1997) reported observations and analysis of the sediment resuspension/saltation produced by NIWs on the Californian continental shelf. Quaresma et al. (2007) studied sediment resuspension by NIWs using data obtained on the Portuguese continental shelf, where the bathymetry and sound speed profile are similar to those at the SW'06 site. It was shown that water turbidity and the concentration of entrained sediment particles in the water changed synchronously with the thermocline displacement. During the maximum thermocline displacement near the leading front of an NIW train, sediment grains were found at far as 35 m from the seafloor. Another example of strong variations in water turbidity due to sediment resuspension by NIWs and formation of an intermediate nepheloid layer were reported by Masunaga et al. (2015). Observations of NIW-induced sediment resuspension are supported by theory and by the results of numerical simulations (Cacchione and Southard, 1974; Bogucki and Redekopp, 1999; Stastna and Lamb, 2008; Olsthoorn and Stastna, 2014; Bourgault et al., 2014).

584 SGN theory, modeling, and experimental data are reviewed by Bassett et al. (2013) and
585 Thorne (2014). SGN theory is based on a model of collisions between two sediment particles or
586 between a particle with a slab (obstacle) (Thorne and Foden, 1988; Bassett et al., 2013; Thorne,
587 2014). The spectrum of the radiated sound has a maximum, and the centroid frequency of SGN
588 $f_r \approx C/D^{0.9}$, where $D$ is an effective diameter of sediment particles and $C$ is a function of their
589 material properties (Thorne, 1986; Bassett et al., 2013). For instance, $f_r > 45$ kHz for siliciclastic
590 particles with diameters in the 350–1750 μm range, which are expected to be mobilized at the
591 SHRU3 site. This should not be interpreted to mean, however, that SGN spectrum is
592 concentrated around the centroid frequency or vanishes in the frequency band of our
593 observations. SGN is very broadband and extends to frequencies orders of magnitude below the
594 centroid frequency $f_r$. An example of existence of significant low-frequency components of SGN
595 is provided by seismic measurements of sediment transport in rivers. Roth et al. (2016) infer
596 sediment transport from seismic SGN in the 5–100 Hz frequency band for sediments with $D_{50}$ =
597 8 cm. The centroid frequency estimates (Thorne, 2014; Bassett et al., 2013) would require 25–30
598 meter "particles" to explain 10 Hz noise.

599 Collisions of two suspended sediment particles are the best studied one (Thorne and
600 Foden, 1988; Thorne, 2014) but not the only source of SGN. Cascades of momentum transfer
601 between several sediment particles, which were documented by Bassett et al. (2013), occur on
602 longer time scales than a collision of two particles and, therefore, generate lower-frequency
603 sound (Thorne and Foden, 1988). Impact of a particle on seabed creates the force chains, which
604 extend in unconsolidated sediments to a depth of many particle radii. Such an impact takes a
605 much longer time than a two-particle collision (Krizou and Clark, 2020) and creates a longer-
606 living acoustic source, thus generating lower-frequency components of SGN.

607 Laboratory measurements of SGN spectrum support the field observations of SGN at
608 frequencies much lower than its centroid frequency, see (Thorne, 1985, 1986) and (Thorne and
609 Foden, 1988). For instance, Fig. 6b in the review paper (Thorne, 2014) shows a long low-
610 frequency tail of the measured SGN spectrum for 750- and 1500-μm particles. The tail is much
611 heavier than predicted by the Thorne and Foden (1988) theory. For 1500-μm particles, PSD at 10
612 kHz decreases by only 4.8 dB from the PSD peak value at about 50 kHz. The low-frequency
613 noise is even more pronounced for the smaller, 750-μm particles, with the PSD decreasing by
614 only 3.7 dB between the peak at 100 kHz and 10 kHz. Thus, results of laboratory measurements
615 indicate that strong SGN is expected to be generated at SHRU3 and SHRU5 locations in the
616 frequency band of our field measurements.

617 Acoustic intensity of SGN increases with current velocity and was found to be an
618 acceptable proxy for bedload transport (Thorne, 2014). Recording and analyzing SGN can serve
619 as minimally invasive, continuous means of measurement for sediment transport and for
620 estimating dimensions of mobile particles (Thorne, 2014). This approach was applied to study
621 sediment transport by various types of water flow, including rivers, tidal currents in straits, and
622 surface gravity wave-induced flows in the surf zone (Thorne, 1986; Mason et al., 2007; Thorne,
623 2014; Geay et al., 2017; Rickenmann, 2017; Petrut et al., 2018). Results of SGN analysis,
624 including estimates of grain size distribution, agree well with the direct sampling methods (Petrut
625 et al., 2018). Observations of NIW-induced noise bursts and identification of SGN as a dominant
626 contribution to their intensity on near-bottom sensors, raise the possibility of extending the
627 passive acoustic measurements of sediment transport to the sediment mobilization by strong
628 NIWs on continental shelves. The inherent ability of the technique to provide long term series of
629 autonomous observations is even more important on continental shelves than for measurements

630 in rivers or in the surf zone. Moreover, measurements of the noise bursts with autonomous,
631 moored, single-hydrophone receivers can potentially contribute to improved quantitative
632 understanding of NIW-induced near-bottom currents as well as NIW amplitudes and their
633 temporal and spatial variability on the continental shelf.

634 Sediment-generated noise has an ambient component, which results from sediment
635 particles' collisions with each other and the seabed, as well as a sensor-related component due to
636 particle impacts on the acoustic sensor or its housing. Observations of sediment transport in
637 rivers with sensors on dry land (Roth et al., 2016) offer clear evidence of the ambient component
638 of SGN. On the other hand, sensors are routinely augmented by pipes and plates to increase
639 particle impacts for the purposes of measuring coarse gravel transport (Thorne, 2014;
640 Rickenmann, 2017). Further research is needed to quantify the relative weight of the ambient and
641 sensor-related components of SGN in the NIW-generated noise bursts and the variation of the
642 weight with distance to the seafloor.

643 Given its high intensity, NIW-induced SGN may present significant challenges for the
644 continuous operation of near-bottom acoustic sensors deployed for underwater communication,
645 detection and tracking of biological or man-made sound sources, or remote sensing of the water
646 column and seabed properties. SGN would be equally detrimental whether ambient or sensor-
647 related. Spectral and spatial characteristics of the NIW-induced noise need to be understood and
648 considered during design and deployment of acoustic systems on continental shelves.

649 In the context of acoustic phenomena associated with the sediment mobilization by
650 NIWs, SW'06 observations have a number of limitations, which make an unambiguous
651 identification of noise generation mechanisms challenging, lessen somewhat the confidence in
652 our interpretation of the type-three noise as SGN, and call for a dedicated field experiment. The

key limitations of the dataset underlying our analysis are the lack of independent measurements of sediment transport or water turbidity to verify sediment mobilization; unavailability of current velocity measurements near the seabed at the exact locations of SHRUs; and absence of high-frequency acoustic measurements encompassing the peak of the SGN spectrum. These limitations emerged, in part, because neither occurrence of NIW-induced noise bursts nor SGN generation by NIWs were anticipated at the time of the SW'06 experiment.

Our results and the above discussion suggest that a dedicated experiment to unambiguously and more fully characterize the NIW-induced SGN on the continental shelf should include contact measurements of sediment properties and sediment transport, a high-frequency ADCP for high-resolution measurements of the current velocity profile as close as a meter or a few meters from the seabed, and acoustic measurements in an extremely broad frequency band from about 1 Hz to above 100 kHz. The sediment, flow velocity, and acoustic measurements should be collocated and conducted at a site, where sediment mobilization by NIWs is expected to occur according to the Wiberg and Smith (1987) or similar model. To distinguish between and separately characterize the ambient and instrument-related components of SGN, one can either simultaneously deploy hydrophones with and without a soft cover, which prevents impacts of sediment particles on the sensor and the mooring, or measure the noise spectrum on a vertical hydrophone array extending from the seabed to beyond the layer with suspended sediment particles.

## VI. CONCLUSIONS

In this study, we used a network of temperature, current velocity, and acoustic sensors deployed on the continental shelf off of New Jersey to relate the occurrence of large, transient increases in acoustic noise intensity (noise bursts) to trains of strongly nonlinear internal waves

676 and, more specifically, to individual localized, soliton-like waves that form the trains. The noise
677 bursts occurred in sequences of 60–80 minutes, the duration of which equals the time it took an
678 NIW train to travel past an observation point on the New Jersey shelf. Individual noise bursts
679 lasted for 5–7 minutes and coincided in time with passage of a single soliton-like internal wave
680 past the hydrophone. Very large increases in the spectral density and broadband intensity of
681 noise, of up to 50 dB relative to background, were observed on hydrophones located 6–7 m
682 above the seafloor. The peak acoustic intensity and the spectral content of the noise bursts were
683 controlled by the amplitude of individual soliton-like internal waves and were most directly
684 related to the velocity of the NIW-induced near-bottom currents.

685 The noise burst emergence and observed variations in their intensity and spectral content
686 with water depth, hydrophone elevation above the seafloor, and NIW amplitude have been
687 tentatively explained in terms of three noise generation mechanisms. The low-frequency (below
688 a few tens of Hertz) component of the noise bursts represents the flow noise that occurs due to
689 advection of turbulent pressure pulsations past an acoustic sensor. Hydrophones lying on the
690 seafloor recorded broadband noise, which resulted from the hydrophones being dragged along
691 the seafloor by NIW-induced currents. The strongest noise bursts were associated with sediment-
692 generated noise (SGN). Acoustic waves are generated when sediment is mobilized by NIW
693 currents, and sediment particles collide with each other, with the stationary seabed, and with
694 acoustic sensors. SGN was most pronounced at frequencies above 2 kHz. A distinctive feature of
695 SGN is its threshold character. NIW-induced near-bottom currents stronger than about 40 cm/s
696 were found to be necessary to initiate SGN. Compared to previously described oceanic
697 observations of SGN in tidal channels and the near-shore surf zone, NIW-induced SGN occurs

on the continental shelf at significantly larger water depths than most previous observations and drastically increases the extent of the seafloor area, where SGN occurrence should be expected.

NIW-generated noise bursts are one of the strongest reported acoustic effects of internal waves in the ocean. The noise bursts may present challenges to continuous acoustic communication and acoustic monitoring of the ocean using near-bottom sensors. On the other hand, measurements of the noise bursts with autonomous, single-hydrophone receivers can potentially contribute to improved quantitative understanding of NIW-induced near-bottom currents and sediment transport by internal waves on the continental shelf. Further research, including dedicated field experiments, is needed to fully characterize the spectrum of NIW-induced acoustic noise, its depth-dependence, relative contributions of the ambient and sensor-related components of sediment generated noise as well as the directivity and correlation properties of the ambient component of the NIW-generated acoustic noise.

## ACKNOWLEDGMENTS

The authors are grateful to A. Serebryany and an anonymous reviewer for their valuable comments, which helped us improve the manuscript. The Shallow Water 2006 experiment was supported by the US Office of Naval Research. The data used in this study were collected by the Woods Hole Oceanographic Institution and can be accessed from http://acoustics.whoi.edu/sw06/. This work was supported by the National Science Foundation grant OCE1657430, Binational Science Foundation grant 2016545, ONR award N00014-20-WX01312, and ONR Global grant N62909-16-1-2079-P00002.

718 **REFERENCES**

719 Apel, J. (**2003**). "A new analytical model for internal solitons in the ocean," J. Phys. Oceanogr.
720 **33,** 2247–2268.

721 Apel, J. R., Ostrovsky, L. A., Stepanyants, Y. A., and Lynch, J. F. (**2007**). "Internal solitons in
722 the ocean and their effect on underwater sound," J. Acoust. Soc. Am. **121**(2), 695–722.

723 Badiey, M., Mu, Y., Lynch, J., Apel, J., and Wolf, S. (**2002**). "Temporal and azimuthal
724 dependence of sound propagation in shallow water with internal waves," IEEE J. Oceanic Eng.
725 **27**(1), 117–129.

726 Badiey, M., Katsnelson, B. G., Lynch, J. F., and Pereselkov, S. (**2007**). Frequency dependence
727 and intensity fluctuations due to shallow water internal waves," J. Acoust. Soc. Am. **122**(2),
728 747–760.

729 Bassett, C., Thomson, J., and Polagye, B. L. (**2013**). "Sediment-generated noise and bed stress in
730 a tidal channel," J. Geophys. Res. Oceans, **118**(4), 2249–2265.

731 Bassett, C., Thomson, J., Dahl, P. H., and Polagye, B. (**2014**). "Flow-noise and turbulence in two
732 tidal channels," J. Acoust. Soc. Am. **135**(4), 1764–1774.

733 Bourgault, D., Morsilli, M., Richards, C., Neumeier, U., and Kelley, D. E. (**2014**). "Sediment
734 resuspension and nepheloid layers induced by long internal solitary waves shoaling orthogonally
735 on uniform slopes," Continental Shelf Res. **72**, 21–33.

736 Bogucki, D., Dickey, T., and Redekopp, L. G. (**1997**). "Sediment resuspension and mixing by
737 resonantly generated internal solitary waves," J. Phys. Oceanogr. **27**(7), 1181–1196.

738 Bogucki, D., and Redekopp, L. (**1999**). "A mechanism for sediment resuspension by internal
739 solitary waves," Geophys. Res. Lett. **26**(9), 1317–1320.

740 Cacchione, D. A., and Southard, J. B. (**1974**). "Incipient sediment movement by shoaling internal
741 gravity waves," J. Geophys. Res. **79**(15), 2237–2242.

742 Carr, M., and Davies, P. A. (**2006**). "The motion of an internal solitary wave of depression over a
743 fixed bottom boundary in a shallow, two-layer fluid," Phys. Fluids, **18**, 016601,
744 doi:10.1063/1.2162033.

745 Colosi, J. A., Scheer, E. K., Flatté, S. M., Cornuelle, B. D., Dzieciuch, M. A., Munk, W. H.,
746 Worcester, P. F., Howe, B. M., Mercer, J. A., Spindel, R. C., and Metzger, K. (**1999**).
747 "Comparisons of measured and predicted acoustic fluctuations for a 3250-km propagation
748 experiment in the eastern North Pacific Ocean," J. Acoust. Soc. Am. **105**(6), 3202–3218.

749 Geay, T., Belleudy, P., Gervaise, C., Habersack, H., Aigner, J., Kreisler, A., Seitz H., and
750 Laronne, J. (**2017**). "Passive acoustic monitoring of bed load discharge in a large gravel bed
751 river," J. Geophys. Res. Earth Surface, **122**(2), 528–545. doi:10.1002/2016JF004112.

752 Godin, O. A., Voronovich, A. G., and Goncharov, V. V. (**2006**). "Refraction of sound in a
753 horizontally inhomogeneous, time dependent ocean," IEEE J. Oceanic Eng. **31**(2), 384–401.

754 Goff, J. A., Kraft, B. J., Mayer, L. A., Schock, S. G., Sommerfield, C. K., Olson, H. C., Gulick,
755 S. P., and Nordfjord, S. (**2004**). "Seabed characterization on the New Jersey middle and outer
756 shelf: correlatability and spatial variability of seafloor sediment properties," Marine Geology,
757 **209**(1-4), 147–172. doi:10.1016/j.margeo.2004.05.030

758 Kaiser, J., and Schafer, R. (**1980**). "On the use of the $I_0$-sinh window for spectrum analysis,"
759 IEEE Trans. Acoust. Speech Signal Processing, **28**(1), 105–107.

760 Katsnelson, B. G., Grigorev, V., Badiey, M., and Lynch, J. F. (**2009**). "Temporal sound field
761 fluctuations in the presence of internal solitary waves in shallow water," J. Acoust. Soc. Am.
762 **126**(1), EL41–EL48.

763 Krizou, N., and Clark, A. H. (**2020**). "Power-law scaling of early-stage forces during granular
764 impact," Phys. Rev. Lett. **124**(17), 178002.

765 Linder, C. A., and Gawarkiewicz, G. (**1998**). "A climatology of the shelfbreak front in the
766 Middle Atlantic Bight," J. Geophys. Res. Oceans **103**, 18405–18423.

767 Lueck, R. G., and Lu, Y. (**1997**). "The logarithmic layer in a tidal channel," Cont. Shelf Res.
768 **17**(14), 1785–1801.

769 Lynch, J., and Tang, D. (**2008**). "Overview of Shallow Water 2006 JASA EL Special Issue
770 Papers," J. Acoust. Soc. Am. **124**(3), EL63–EL65.

771 Mason T., Priestley D., and Reeve, D. E. (**2007**). "Monitoring near-shore shingle transport under
772 waves using a passive acoustic technique," J. Acoust. Soc. Am. **122**(2), 737–746.

773 Masunaga, E., Homma, H., Yamazaki, H., Fringer, O. B., Nagai, T., Kitade, Y., and Okayasu, A.
774 (**2015**). "Mixing and sediment resuspension associated with internal bores in a shallow bay,"
775 Cont. Shelf Res. **110**, 85–99.

776 Miller, M. C., McCave, I. N., and Komar, P. (**1977**). "Threshold of sediment motion under
777 unidirectional currents," Sedimentology, **24**(4), 507–527.

778 Newhall, A. E., Duda, T. F., von der Heydt, K., Irish, J. D., Kemp, J. N., Lerner, S. A.,
779 Liberatore, S. P., Lin, Y. T., Lynch, J. F., and Maffei, A. R. (**2007**). Acoustic and oceanographic
780 observations and configuration information for the WHOI moorings from the SW06 experiment.
781 Technical Report No. WHOI-2007-04. (Woods Hole Oceanographic Institution, MA) 116 pp.

782 Newhall, A. E., Lin, Y.-T., Lynch, J. F., Baumgartner, M. F., and Gawarkiewicz, G. G. (**2012**).
783 "Long distance passive localization of vocalizing sei whales using an acoustic normal mode
784 approach," J. Acoust. Soc. Am. **131**(2), 1814–1825.

785 Olsthoorn, J., and Stastna, M. (**2014**). "Numerical investigation of internal wave-induced
786 sediment motion: Resuspension versus entrainment," Geophys. Res. Lett. **41**(8), 2876–2882.

787 Petrut, T., Geay, T., Gervaise, C., Belleudy, P., and Zanker, S. (**2018**). "Passive acoustic
788 measurement of bedload grain size distribution using self-generated noise," Hydrology Earth
789 System Sci. **22**(1), 767–787.

790 Rickenmann, D. (**2017**). "Bed-load transport measurements with geophones and other passive
791 acoustic methods," J. Hydraulic Eng. **143**(6), 03117004.

792 Roth, D. L., Brodsky, E. E., Finnegan, N. J., Rickenmann, D., Turowski, J. M., and Badoux, A.
793 (**2016**). "Bed load sediment transport inferred from seismic signals near a river," J. Geophys.
794 Res. Earth Surface, **121**(4), 725–747. doi:10.1002/2015JF003782.

795 Serebryany, A. N., Furduev, A. V., Aredov, A. A., and Okhrimenko, N. N. (**2005**). "Ambient
796 noise generated by large-amplitude internal waves in the ocean," Doklady Earth Sci. **402**(4),
797 654–657.

798 Serebryany, A. N., Newhall, A., and Lynch, J. F. (**2008a**). "Observations of noise generated by
799 nonlinear internal waves on the continental shelf during the SW06 experiment," J. Acoust. Soc.
800 Am. **123**(5), 3589–3589.

801 Serebryany, A., Lynch, J., and Newhall, A. (**2008b**). "Underwater noise generation by nonlinear
802 internal waves on the Atlantic shelf of USA during the experiment "SHALLOW WATER
803 2006"," Proc. Russian Acoust. Soc. **9**, 217–227.

804 Shroyer, E. L., Moum, J. N., and Nash, J. D. (**2009**). "Observations of polarity reversal in
805 shoaling nonlinear internal waves," J. Phys. Oceanogr. **39**(3), 691–701.

806 Shroyer, E. L., Moum, J. N., and Nash, J. D. (**2011**). "Nonlinear internal waves over New
807 Jersey's continental shelf," J. Geophys. Res. Oceans, **116**, C03022. doi:10.1029/2010JC006332.

808 Simmen, J., Flatté, S. M., and Wang, G. Y. (**1997**). "Wavefront folding, chaos, and diffraction
809 for sound propagation through ocean internal waves," J. Acoust. Soc. Am. **102**(1), 239–255.

810 Stastna, M., and Lamb, K. G. (**2008**). "Sediment resuspension mechanisms associated with
811 internal waves in coastal waters," J. Geophys. Res. Oceans, **113**(C10), C10016.

812 Strasberg, M. (**1979**). "Nonacoustic noise interference in measurements of infrasonic ambient
813 noise," J. Acoust. Soc. Am. **66**(5), 1487–1493.

814 Tang, D., Moum, J. N., Lynch, J. F., Abbot, P., Chapman, R., Dahl, P. H., Duda, T. F.,
815 Gawarkiewicz, G., Glenn, S., Goff, J. A., Graber, H., Kemp, J., Maffei, A., Nash, J. D., and
816 Newhall, A. (**2007**). "Shallow Water '06: A joint acoustic propagation/nonlinear internal wave
817 physics experiment," Oceanography, **20**(4), 156–167. https://doi.org/10.5670/oceanog.2007.16.

818 Thorne, P. D. (**1985**). "The measurement of acoustic noise generated by moving artificial
819 sediments," J. Acoust. Soc. Am. **78**(3), 1013–1230.

820 Thorne, P. D. (**1986**). "Laboratory and marine measurements on the acoustic detection of
821 sediment transport," J. Acoust. Soc. Am. **80**(3), 899–910.

822 Thorne, P. D. (**2014**). "An overview of underwater sound generated by interparticle collisions
823 and its application to the measurements of coarse sediment bedload transport," Earth Surf. Dyn.
824 **2**(2), 531–543.

825 Thorne, P. D., and Foden, D. J. (**1988**). "Generation of underwater sound by colliding spheres,"
826 J. Acoust. Soc. Am. **84**, 2144–2152.

827 Voulgarist, G., Workman, M., and Collins, M. (**1999**). "Measurement techniques of shingle
828 transport in the nearshore zone," J. Coastal Res. **15**(4), 1030–1039.

829 Webb, S. C. (**1988**). "Long-period acoustic and seismic measurements and ocean floor currents,"
830 IEEE J. Oceanic Eng. **13**(4), 263–270.

831 Wenz, G. M. (**1962)**. "Acoustic ambient noise in the ocean: spectra and sources," J. Acoust. Soc.
832 Am. **34** (12), 1936–1956.

833 Wiberg, P. L., and Smith, J. D. (**1987**). "Calculations of the critical shear stress for motion of
834 uniform and heterogeneous sediments," Water Resources Res. **23**(8), 1471–1480.

835 Xue, J., Graber, H. C., Romeiser, R, and Lund, B. (**2014**). "Understanding internal wave-wave
836 interaction patterns observed in satellite images of the Mid-Atlantic Bight," IEEE Trans. Geosci.
837 Remote Sensing, **52**(6), 3211–3219.

838 Yang, Y. J., Chan, H. C., Wu, J. C. H., Liang, W. D., Chen, C. F., and Wei, R. C. (**2013**). "Ocean
839 ambient noises modulated by internal solitary waves," in: *2013 MTS/IEEE OCEANS-Bergen,*
840 *Norway* (IEEE, Bergen), pp. 1–4. doi:10.1109/OCEANS-Bergen.2013.6608073.

841 Yang, Y. J., Chiu, C. S., Wu, J. C. H., Liang, W. D., Ramp, S. R., Reeder, D. B., and Chen, C. F.
842 (**2015**). "Observations of ambient noises induced by the internal solitary waves on the
843 continental slope of the northern South China Sea: Ambient noises by ISW in SCS," in:
844 *OCEANS 2015-Genova, Italy* (IEEE, Genova), pp. 1–4. doi:10.1109/OCEANS-
845 Genova.2015.7271579.

Zhou, J. X., Zhang, X. S., and Rogers, P. (**1991**). "Resonant interaction of sound waves with internal solitons in the coastal zone," J. Acoust. Soc. Am. **90**(4), 2042–2054.

849 **Figure 1**. Evolution of a train of nonlinear internal waves over the site of the Shallow Water
850 2006 (SW'06) experiment. Positions of thermistor chains SW01, SW03, SW04, SW07, SW23,
851 SW 24, SW30, SW54, single-hydrophone acoustic receivers SHRU1, SHRU 2, SHRU3,
852 SHRU4, SHRU5 and hydrophone array HVLA Shark as well as wave fronts (dashed lines) and
853 the direction of propagation (arrow) of an internal wave train are indicated in the map in the
854 lower left corner. Bathymetry is shown along the straight line through SW01 and SW24. ADCP
855 is located at the SW30. Depth dependence of water temperature as measured by SW01 (**a**),
856 SW03 (**b**), SW04 (**c**), SW54 (**d**), and SW23 (**e**) is shown from 07:00 to 21:00 GMT on 19
857 August 2006 when a train of nonlinear internal waves propagated shoreward from SW23 past
858 SW01. Time (GMT) on 19 August 2006 is shown in hours and minutes.

859 **Figure 2**. Time histories of water temperature and acoustic intensity at various points along the
860 path of propagating internal wave train. Temperature records of thermistors at the depth of 40 m
861 are denoted by letter T and depicted in red for thermistor chains SW23, SW54, SW04, SW03,
862 and SW01. Time intervals of appearance of the NIW train are denoted t1, t2, t3, t4 for the last
863 four chains (SW23 does not show NIWs) and boxed. Sound intensity records by SHRUs 1, 3, 4,
864 and 5 and hydrophone 40 of HVLA Shark are depicted in blue. For visibility, the time
865 dependencies recorded by individual sensors are shifted vertically in proportion to the distance
866 from the sensor to SW01. Time intervals with strong fluctuations of acoustic pressure are boxed
867 and marked ***a*** for SHRU1, ***b*** for HVLA Shark, ***c*** for SHRU3, ***d*** SHRU4, and *e* SHRU5. Time
868 (GMT) on 19 August 2006 is shown in hours and minutes. Five color panels in the lower part of
869 the figure show the spectrograms corresponding to the sound intensity records in boxes ***a***–***e***.

870 **Figure 3**. Temperature, current velocity, and acoustic manifestations of an NIW train in the
871 vicinity of the acoustic receiver SHRU3. (**a**) Spectrogram of acoustic noise recorded by SHRU3.

872 (**b**) Time history of the water temperature on the thermistor chain SW07. (**c**) Time history of the
873 water temperature on the thermistor chain SW30. (**d**) Time-dependence of the horizontal current
874 velocity at three depths. Time (GMT) on 19 August 2006 is shown in hours and minutes.

875 **Figure 4**. Temporal variations of the temperature depth dependence measured by thermistor
876 chain SW54 (upper panel) and noise intensity on a collocated hydrophone (lower panel). Time
877 (GMT) on 19 August 2006 is shown in hours and minutes.

878 **Figure 5**. Temporal variation of the acoustic intensity measured by SHRU5. Time (GMT) on 19
879 August 2006 is shown in hours and minutes. The insert shows the spectrogram of a nine-minute
880 section of the pressure record and illustrates contributions of research sound sources. Color
881 shows power spectral density of total acoustic field in dB re 1 $\mu Pa^2/Hz$.

882 **Figure 6**. Spectrograms of acoustic field recorded by hydrophones on vertical (VLA) and
883 horizontal (HLA) arrays during passage of a train of nonlinear internal waves. Spectrograms are
884 shown of acoustic pressure on a VLA hydrophone at depth of 62 m (**a**); low-frequency part of
885 the acoustic pressure on the same hydrophone (**b**); on a hydrophone in the middle of HLA (**c**);
886 and on single-hydrophone receiver SHRU5 (**d**). Time (GMT) on 19 August 2006 is shown in
887 hours minutes, and seconds.

888 **Figure 7.** Theoretical estimates of the threshold of sediment mobilization by near-bottom
889 currents. **(a)** The minimum value $u_*^{cr}$ of the shear velocity $u_*$ that leads to mobilization of
890 sediment grains of size $D$ is depicted under the conditions of the SW'06 experiment, where $k_s$ =
891 0.035 cm (1), and for seabeds with three other roughness scales: $k_s$ = 0.02 cm (2), 0.07 cm (3),
892 and 0.10 cm (4). The threshold $u_*^{cr}$ values are calculated following Wiberg and Smith (1987).

Also shown is the Inman curve (5), which gives an experimentally determined $u_*^{cr}$ for well-sorted seabeds with $k_s = D$. The Inman curve is adapted from (Miller et al., 1977) and (Wiberg and Smith, 1987). **(b)** ADCP-measured time-dependence of the horizontal current velocity at depth of 68.3 m. Thin horizontal lines show theoretical values of the minimum current velocity required for mobilization of the poorly sorted sediments of the four different sediment types considered in (a). Time (GMT) on 19 August 2006 is shown in hours and minutes.

**Figure 8**. Power spectra of acoustic pressure recorded by SHRU5 and hydrophones on vertical and horizontal arrays when nonlinear internal waves are absent (**a**) or present (**b**). The power spectra are calculated for the same hydrophones as in Fig. 6.